BNL-222382-2021-JAAM

Dynamic mode decomposition of random pressure fields over bluff bodies

X. Luo

To be published in "Journal of Engineering Mechanics "

April 2021

Computational Science Initiative

Brookhaven National Laboratory

U.S. Department of Energy

USDOE Office of Science (SC), Advanced Scientific Computing Research (SC-21)

DISCLAIMER

Dynamic mode decomposition of random pressure fields over bluff bodies

Xihaier Luo[1] and Ahsan Kareem[2]

[1]Ph.D. Candidate, NatHaz Modeling Laboratory, Univ. of Notre Dame, 156 Fitzpatrick Hall, Notre Dame, IN 46556. Email: xluo1@nd.edu

[2]Robert M. Morgan Professor, NatHaz Modeling Laboratory, Univ. of Notre Dame, 156 Fitzpatrick Hall, Notre Dame, IN 46556. Email: kareem@nd.edu

ABSTRACT

Fluctuating surface pressures on a bluff body exposed to a boundary layer flow are generally characterized as a spatiotemporally varying random field. In this paper, a dynamic mode decomposition (DMD) is applied to extract dominant features embedded in these random pressure fields. Utilizing an unsupervised machine learning algorithm, spatial modes, as well as their temporal variations, are grouped into different clusters at scales, e.g., macro, meso, and micro. A proper orthogonal decomposition (POD) of the experimental data is also carried out to observe commonalities and distinctive perspectives each decomposition offers. A comprehensive examination of the DMD/POD for their convergence criteria, data sufficiency, and analysis of modal components is conducted. The physical interpretation of the spatiotemporal pressure field based on these decomposition schemes is discussed. The DMD modes at different scales can capture the evolution of aerodynamic features, e.g., convection of vortices (or vortex tubes) and other structures. The distribution of energy among these three broad scales also reflects an energy cascade in pressure fluctuations akin to turbulence.

INTRODUCTION

The advancement in new light-weight materials and construction technologies have resulted in the emergence of extremely slender and tall modern buildings worldwide. Such tall building

structures, usually with a high height-to-breath aspect ratio, are very susceptible to dynamic wind load effects and glass/facade damages (Chen and Kareem 2004; Huang and Chen 2007; Cui and Caracoglia 2018). Most megacities continue to expand in the vertical direction due to bounded horizontal space. To ensure the structural performance and serviceability of tall buildings, wind tunnel tests continue to be the leading practical way at this juncture to provide reliable studies of wind effects on tall buildings (Vickery 1966; Lee 1975; Cermak 1976; Tanaka et al. 2012; Kim et al. 2018), with emerging capabilities being offered by computational fluid dynamics (Ding et al. 2019).

To date, experimental analysis of the dynamic wind forces acting on tall buildings has benefited from the advances in pressure transducer design, synchronous acquisition schemes, and data management. However, measurements that capture wind-structure interactions often are high-dimensional and contain noise. Moreover, the fluctuating wind pressures on the model surfaces are caused by unsteady aerodynamics including the influence of incoming turbulence, unsteady flow separation and reattachment, etc (Carassale and Solari 2002; Chen 2013; Solari 2016). These complex interactions lead to the question of how to distill useful information from experimental data to better understand the evolution of the pressure field and its impact.

A common practice to analyze aerodynamics of bluff bodies, e.g., a finite-height square prism representing a tall building, is to extract physically important features, or similar modes to explain the dynamics of wind loading. The most widely used approach in dealing with spatialtemporally varying random wind pressure fields is the proper orthogonal decomposition (POD), e.g., (Kareem and Cermak 1984; Tamura et al. 1999; Carassale et al. 2001; Chen and Kareem 2005b; Solari et al. 2007). In general, POD analysis involves a procedure that transforms a random field into a set of uncorrelated spatial modes that are orthogonal in space. The transformation is based on least squares minimization, that is, POD optimally evaluates the random pressure field in a L_2 norm sense. Hence, the first few modes ranked on the basis of the proportional energy are usually sufficient to recover the underlying dynamics. Despite its wide range of applications, POD analysis is restricted to estimating the second-order statistics, and its reduced-dimension representation is

limited to a linear transformation range (Aubry et al. 1988; Berkooz et al. 1993). More importantly, Vanilla POD mixes together multiple frequencies (Muld et al. 2012b; Muld et al. 2012a; Zhang et al. 2014; Bistrian and Navon 2015; Taira et al. 2017; Towne et al. 2018; Zhao et al. 2019), namely, a POD mode may contain a continuous frequency spectrum with energy distributed over a broader range of frequencies (See Fig. 1).

One of the essential upcoming approaches for addressing the mixed temporal frequencies issue encountered in POD analysis is to integrate the *flow map*, which gives rise to a continuous evolution of underlying fluctuating wind pressure dynamics, into the decomposition process. This is the central idea of the operator-theoretic modeling, especially the Koopman operator that lifts underlying dynamics from the description in the state space to the space of *observables*, which are functions of the state variables (Koopman 1931; Mezić 2005; Budišić et al. 2012). The nonlinear, finite-dimensional pressure dynamics is mapped into a linear but infinite-dimensional Hilbert space via the Koopman operator. Solving such an infinite-dimensional representation, however, can be very challenging. Different methods have been developed recently to obtain a numerical approximation of the Koopman operator. Dynamic mode decomposition (DMD), which is an equation-free method and was initially introduced by Schmid (Schmid 2010) out of a need to identify spatio-temporal patterns buried in fluid flows, was found closely connected to the spectral analysis of the Koopman operator (Rowley et al. 2009; Chen et al. 2012; Tu et al. 2013; Williams et al. 2015; Dawson et al. 2016; Giannakis 2019). Specifically, DMD decomposes a linearly dependent operator that is determined by a pair of time-shifted matrices to approximate the spectral properties associated with the Koopman operator. This results in a group of periodically oscillating eigenmodes.

In this study, DMD is applied to identify the most dominant wind pressure patterns along with their time variations. The computed POD and DMD results are complementary in the interpretations of pressure fields over bluff bodies. Compared to POD, results indicate DMD is able to isolate identified coherent structures with a specific frequency as well as a corresponding temporal growth/decay. Fig. 1 highlights the distinguishing features of these decompositions.

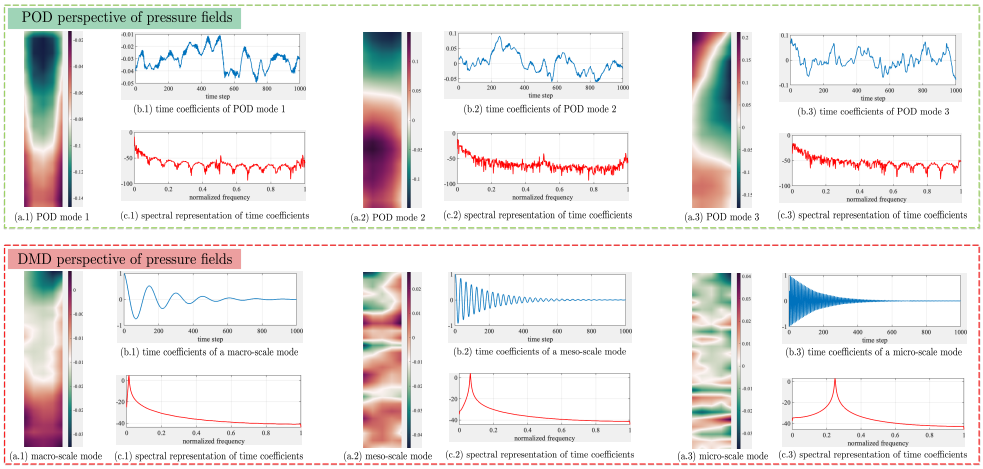

Fig. 1. Decomposition analysis for aerodynamic characteristics of a prism. The temporal behavior of POD modes contain a mix of frequencies while DMD can isolate each spatial pattern with a dominant frequency (See the spectrum of identified modes).

The contribution of this work is three-fold. First, the aerodynamic characteristics of fluctuating surface pressures have been examined in detail. A comparative study of POD and DMD computed using experimental pressure fields over surfaces of a scaled model of a finite height prism is carried out. Second, experimental data has been embedded in a higher dimensional Euclidean space by means of Takens' embedding, where the topological properties stay unchanged while the underlying dynamics has been unfolded in a more identifiable form for DMD analysis (Takens 1981; Brunton et al. 2017; Le Clainche and Vega 2017). Third, an unsupervised learning approach based on clustering is utilized to group similar DMD modes into the same cluster (Arthur and Vassilvitskii 2007; Murphy 2012). More importantly, similarities between clustered DMD modes and approach wind conditions have been noticed, which have led to a parallel examination of turbulence and cascading features of surface pressure fluctuations.

The remainder of this paper is organized as follows. Section. 2 presents the problem we are dealing with and offers a detailed discussion on the solution method. Section. 3 describes the experimental setup of the comparative case study. Subsequently, Section. 4, Section. 5, and Section. 6 summarize the POD/DMD results including algorithm convergence, data sufficiency, and modal analysis. Finally, concluding remarks and an outlook on future work are provided

in Section. 7. All codes, decomposition models and experimental data used in this work are open-sourced for full reproducibility [1].

METHODOLOGY

In this work, the primary focus is on analyzing the fluctuating wind pressures over a prism. From a dynamical evolution perspective, the experimental data can be formulated as:

$$\boldsymbol{x}_k = \mathbf{F}\left(\boldsymbol{x}_{k-1}\right) = \boldsymbol{x}_{k-1} + \int_{t_{k-1}}^{t_k} f\left(\tau, \boldsymbol{x}\left(\tau\right)\right) d\tau \tag{1}$$

with $\boldsymbol{x} \in \mathcal{X} \subset \mathbb{R}^m$ where $\mathcal{X}$ is an open set in $\mathbb{R}^m$. Note $\boldsymbol{x}$ is the wind pressure distribution, m is the number of pressure taps, k denotes the temporal index, τ is a sufficiently small number, and $\mathbf{F}(\cdot)$ is a *flow map* that determines the evolution dynamics of wind pressures from one state to another $\boldsymbol{x}_1 \overset{\mathbf{F}(\cdot)}{\longmapsto} \boldsymbol{x}_2 \overset{\mathbf{F}(\cdot)}{\longmapsto} \ldots \overset{\mathbf{F}(\cdot)}{\longmapsto} \boldsymbol{x}_n$ with n denoting the measured point number.

The objective is to provide physical insights concerning the aerodynamic characteristics contained in $\mathbf{F}(\cdot)$ by analyzing $\mathcal{D} = [\boldsymbol{x}_1, \ldots, \boldsymbol{x}_n]$. Because the pressure data is highly nonlinear and exhibits multi-scale pattern in both space and time (Huang and Chen 2007; Tanaka et al. 2012; Carassale and Brunenghi 2011; Chen and Kareem 2005a), an operator-theoretic approach is considered in the following.

Background: the Koopman operator

Consider a dynamical system given in Eq. 1, the operator-theoretic approach considered in this paper is the Koopman operator $\mathcal{K}(\cdot)$, which by definition is an infinite-dimensional linear operator that acts on the so-called *observables* g as (Budišić et al. 2012; Williams et al. 2015; Arbabi and Mezic 2017; Klus et al. 2015):

$$\mathcal{K}_t g = g \circ \mathbf{F}_t \tag{2}$$

where $\circ$ denotes the composition operation. By combining Eq. 1 and Eq. 2, the dynamics of interest can be expressed as:

[1]Code available at: https://xihaier.github.io/

$$\mathcal{K}_{\Delta t} g(\boldsymbol{x}_k) = g(\mathbf{F}_{\Delta t}(\boldsymbol{x}_k)) = g(\boldsymbol{x}_{k+1}) \tag{3}$$

In general, *observables* denotes a set of real-valued measurement function $g : \mathcal{X} \rightarrow \mathbb{R}$. The Koopman operator lifts the nonlinear wind pressure dynamics from the finite-dimensional space $\mathcal{X}$ to the space of *observables*, that is, an infinite-dimensional Hilbert space, and hence produces a linear evolution expression of nonlinear dynamics:

$$g(\boldsymbol{x}_{k+1}) = \mathcal{K}_{\Delta t} g(\boldsymbol{x}_k) \tag{4}$$

Spectral properties of the Koopman linear operator $\mathcal{K}$ can capture nonlinear pressure dynamics of interest, in particular, by identifying harmonic components from collected dataset (Bistrian and Navon 2015; Rowley et al. 2009; Chen et al. 2012). Accordingly, each *observable* may be expanded in terms of identified components:

$$g(\boldsymbol{x}) = \sum_{i=1}^{\infty} \varphi_i(\boldsymbol{x}) \mathbf{a}_i \tag{5}$$

where $\mathbf{a}_i$ are mode amplitiudes and $\varphi_i(\boldsymbol{x})$ are so-called Koopman eigenfunctions that span the subspace of the *observable* at a given instant k:

$$g(\boldsymbol{x}_k) = \sum_{i=1}^{\infty} \lambda_i^k \varphi_i(\boldsymbol{x}_0) \mathbf{a}_i \quad \text{where} \quad \lambda_i = \exp(\sigma_i + j\omega_i) \tag{6}$$

with λ_i denoting the i^{th} Ritz eigenvalue. σ_i is the growth rate and ω_i is the corresponding frequency.

Numerical implementation: data-driven DMD

Becase the Koopman operator $\mathcal{K}$ is an infinite-dimensional linear operator, developing an efficient algorithm for the approximate computation of Koopman eigenfunctions is important (Koopman 1931; Budišić et al. 2012; Lusch et al. 2018; Kutz et al. 2016). In this paper, dynamic mode decomposition (DMD) in augmented input space is considered. From a data-driven modeling

perspective, the basic premise of DMD is the existence of a linear mapping, which advances the wind pressures in time (Schmid 2010; Rowley et al. 2009; Chen et al. 2012; Tu et al. 2013):

$$\boldsymbol{x}_{i+1} = \mathcal{A}\boldsymbol{x}_i \quad \text{where} \quad i = 1, 2, \ldots, n-1 \tag{7}$$

Hence, a snapshot matrix can be formulated as a Krylov series using measured data:

$$\mathbf{X}^n = [\boldsymbol{x}_1, \mathcal{A}\boldsymbol{x}_1, \mathcal{A}^2\boldsymbol{x}_1, \ldots, \mathcal{A}^{n-1}\boldsymbol{x}_1] = \mathcal{A}\mathbf{X}^{n-1} \tag{8}$$

where $\mathbf{X}^{n-1} = [\boldsymbol{x}_1, \ldots, \boldsymbol{x}_{n-1}]$ and $\mathbf{X}^n = [\boldsymbol{x}_2, \ldots, \boldsymbol{x}_n]$. When n is sufficiently large, state space vectors $\boldsymbol{x}_1, \boldsymbol{x}_2, \ldots$ become linearly dependent, and a Galerkin projection of $\mathcal{A}$ onto the subspace spanned by these vectors can be performed to extract the dynamic characteristics associated with $\mathcal{A}$. Similar to the Arnoldi algorithm (Schmid 2010; Rowley et al. 2009; Klus et al. 2015), the n^{th} snapshot can be described utilizing the previous snapshots by:

$$\boldsymbol{x}_n = c_1\boldsymbol{x}_1 + c_2\boldsymbol{x}_2 + \cdots + c_{n-1}\boldsymbol{x}_{n-1} + \mathcal{R} = \mathbf{X}^{n-1}\mathbf{c} + \mathcal{R}\mathbf{e}^T \tag{9}$$

where $\mathcal{R}$ is the residual vector, $\mathbf{c}$ is the unknown coefficients vector, and $\mathbf{e}$ is the Euclidean unit vector. Following the matrix notation stated in Eq. 8, Eq. 9 writes as:

$$\mathcal{A}\mathbf{X}^{n-1} = \mathbf{X}^n = \mathbf{X}^{n-1}C + \mathcal{R}\mathbf{e}^T \quad \text{where} \quad C = \begin{bmatrix} 0 & 0 & \cdots & 0 & c_1 \\ 1 & 0 & \cdots & 0 & c_2 \\ 0 & 1 & \cdots & 0 & c_3 \\ \vdots & & \ddots & & \vdots \\ 0 & 0 & \cdots & 1 & c_n \end{bmatrix} \tag{10}$$

with C denoting the companion matrix. Spectral properties of C are known to approximate eigenvalues and eigenvectors of the high-dimensional system matrix $\mathcal{A}$ (Muld et al. 2012a; Zhang et al. 2014), capturing dominant behaviors of fluctuating wind pressures. Numerical schemes for determining the companion matrix include QR-decomposition, SVD, etc (Schmid 2010; Rowley

et al. 2009; Chen et al. 2012; Tu et al. 2013). An SVD-based implementation scheme often referred to as the data-driven DMD algorithm is summarized here:

1. Perform the singular value decomposition of $\mathbf{X}^n$, letting $\mathbf{X}^n = \mathbf{U}\mathbf{\Sigma}\mathbf{V}^*$.
2. Build a low-rank truncation by $\mathbf{U}_r = \mathbf{U}[:, 1:r], \mathbf{V}_r = \mathbf{V}[:, 1:r], \mathbf{\Sigma}_r = \mathbf{\Sigma}[1:r, 1:r]$. Note that this is optional.
3. Estimate $\mathcal{A}$ using the Moore-Penrose pseudoinverse of $\mathbf{X}^{n-1}$:

$$\tilde{\mathcal{A}} = \boldsymbol{U}_r^* \mathbf{X}^n \boldsymbol{V}_r \mathbf{\Sigma}_r^{-1} \tag{11}$$

4. Compute the eigendecomposition of $\tilde{\mathcal{A}}$:

$$\tilde{\mathcal{A}}\mathbf{\Phi} = \mathbf{\Phi}\mathbf{\Lambda} \tag{12}$$

   where columns of $\mathbf{\Phi} = [\phi_1, \phi_2, \dots]$ are eigenvectors and $\mathbf{\Lambda}$ is a diagonal matrix containing complex eigenvalues.
5. Determine the DMD modes by:

$$\boldsymbol{\varphi} = \mathbf{X}^n \boldsymbol{V}_r \mathbf{\Sigma}_r^{-1} \mathbf{\Phi} \tag{13}$$

   It should be addressed that DMD modes computed by Eq. 13 are often called exact DMD modes and one can also perform the calculation as $\boldsymbol{\varphi}' = \mathbf{U_r}\mathbf{\Phi}$, where $\boldsymbol{\varphi}'$ are usually referred to as projected DMD modes.

To improve the accuracy of extracted DMD modes from noisy wind tunnel data, Takens' embedding is considered to enrich the pressure dataset, i.e. the snapshot matrix $\mathcal{D} = [\boldsymbol{x}_{t_1}, \boldsymbol{x}_{t_2}, \dots, \boldsymbol{x}_{t_n}]$ defined in Eq. 8. In particular, in the analysis of fluctuating wind pressure over a finite prism with limited sensors, a Hankel matrix is populated by stacking the elements of time-delayed coordinates (Takens 1981; Brunton et al. 2017; Le Clainche and Vega 2017):

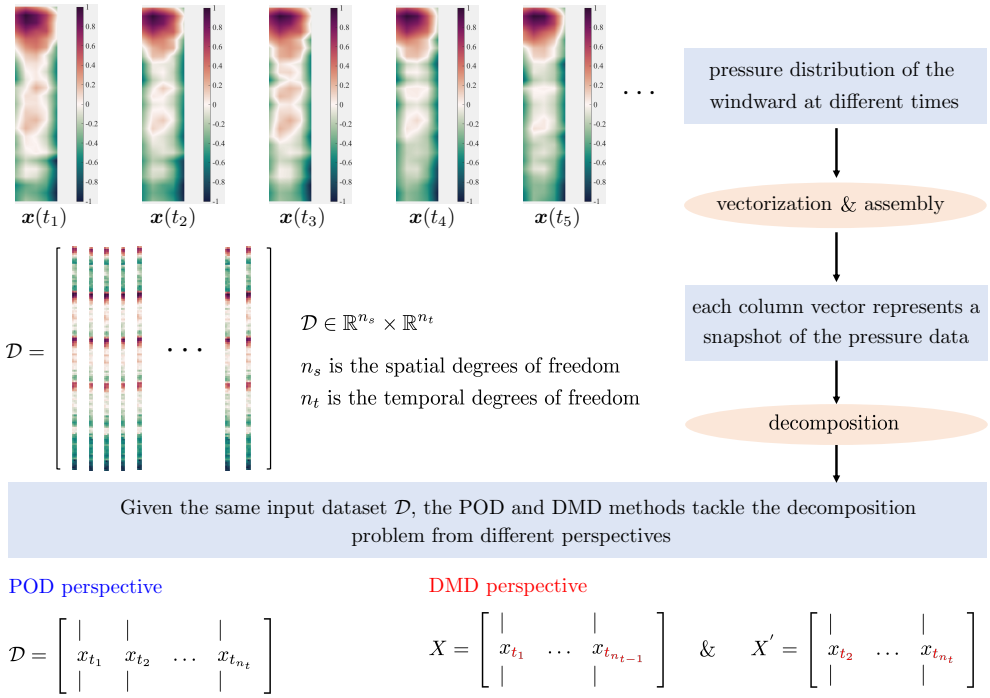

Fig. 2. Schematic illustration of data-driven decomposition methods.

$$\mathbf{H} = [\boldsymbol{h}_1, \boldsymbol{h}_2, \ldots, \boldsymbol{h}_j] \triangleq \begin{bmatrix} \boldsymbol{x}_{t_1} & \boldsymbol{x}_{t_2} & \ldots & \boldsymbol{x}_{t_j} \\ \boldsymbol{x}_{t_2} & \boldsymbol{x}_{t_3} & \ldots & \boldsymbol{x}_{t_{j+1}} \\ \vdots & \vdots & \ddots & \vdots \\ \boldsymbol{x}_{t_i} & \boldsymbol{x}_{t_{i+1}} & \ldots & \boldsymbol{x}_{t_{i+j-1}} \end{bmatrix} \tag{14}$$

where the i indicates the embedding number. Consequently, a pair of time-shifted matrices $\mathbf{H}^{j-1}$ and $\mathbf{H}^{j}$ can be defined and the aforementioned data-driven DMD algorithm will take this augmented pair as new input for decomposition. Fig. 2 graphically summarizes the workflow.

Remark 1 Before analyzing wind tunnel data, a synthetic dynamic system is studied to highlight the difference between DMD and other commonly used decompositions, i.e., POD and ICA. It is included in the Appendix.

CASE STUDY

Wind tunnel data

The case study analyzes a aerodynamic pressure field over a finite prism of with dimensions of $0.5m \times 0.1m \times 0.1m$ immersed in a boundary layer flow. The experimental dataset was collected from an open-circuit wind tunnel of dimensions $14m \times 1.2m \times 1.0m$ (TPU). Specifically, the approach flow mean speed profile along the height was defined by a power law exponent of $1/4$, and tests were conducted at a wind speed of $11.1438\,m/s$. To measure the pressure, 500 sensors have been installed on the scaled model. As a result, there were 125 sensors uniformly distributed on each surface, that is, a 5×25 distribution pattern in terms of the horizontal and vertical axis, respectively. All pressure taps were synchronously recorded at a sampling frequency of $1000\,Hz$ for a sample period of $32.768\,s$. For a better examination of these decompositions, the collected pressure data was transformed into conventional pressure coefficients. For more information about the wind tunnel data, please refer to TPU database.

Case study outline

The case study is a comprehensive comparative analysis of POD and DMD with an emphasis on DMD for identifying dynamical pressure patterns and for better understanding of the aerodynamics of wind-structure interactions. Three types of analyses have been performed.

Convergence Analysis Because the wind tunnel data $\mathcal{D}$ consists of 32768 snapshots in total, a reasonable number N_{snap} of snapshots is crucial for efficient computation. The objective of the convergence study is to determine how many snapshots are required to ensure the decomposition results are unaffected by changing the number of snapshots (Muld et al. 2012b; Muld et al. 2012a). For instance, a small N_{snap} (e.g. $N_{snap} = 30$) may not achieve converged results while a large N_{snap} (e.g. $N_{snap} = 30000$) would require an additional computation. Two evaluation metrics are defined to measure convergence (See the Appendix). The investigation results are summarized in Section. 4.

Sufficiency Analysis For POD, the goal is to investigate how many modes are needed to reconstruct the matrix representation of the fluctuating wind pressures (Carassale and Solari 2002; Chen and Kareem 2005b; Solari et al. 2007), whereas for DMD, it is to determine the embedding dimen-

sion, i.e., one has to select an embedding number in such a way that the assembled Hankel matrix contains sufficient information for learning underlying aerodynamic characteristics (Le Clainche and Vega 2017; Kutz et al. 2016). For this reason, we investigated the distribution of POD/DMD eigenvalues. The examination of results is presented in Section. 5.

Modal Analysis DMD results have been explained from both spatial and temporal perspectives and compared to POD results. Physically meaningful linkages between DMD modes and dominant flow features, namely, vortex shedding and cascading of energy among various scales of DMD modes (See Section. 6 for details). It should be noted that pressure data at the wind direction $\alpha = 0^{\circ}$ was used in this study, where analyses have been carried out for four surfaces of the prism. For the sake of brevity, decomposition results of the windward surface with some features from the side faces have been summarized in this paper. We report the complete results in the supplementary material, which is available at link.

PART 1: CONVERGENCE STUDY RESULTS

POD Results

Fig. 3 shows the convergence behavior of POD modes and eigenvalues respectively. The first evaluation metric given in the appendix points out the first two fundamental POD modes exhibit consistent convergence properties. It decreases dramatically during the first 1000 time steps $[0, 1000\Delta t]$. On the contrary, higher POD modes ϕ_j^{POD} $(j = 3, \ldots, 7)$ not only converge at a slightly slower pace but also show more random fluctuations. This is in agreement with findings of other studies that incoherent noise tends to dominate and even likely appear as higher-order POD modes (Aubry et al. 1988; Berkooz et al. 1993). Thus, POD is often employed as a truncation method for noise filtering and order reduction (Solari et al. 2007; Taira et al. 2017).

On the other hand, the second evaluation metric is defined as a function of the computed eigenvalues (See the appendix). It is known that the normalized eigenvalues $\lambda_j^{\dagger}$ represent the mean energy distribution of the fluctuating wind pressure data (Cui and Caracoglia 2018; Tamura et al. 1999; Lin et al. 2005; Baker 2000). Shown in Fig. 3, some POD modes have similar energy distribution as their corresponding converged eigenvalues are almost identical. From a

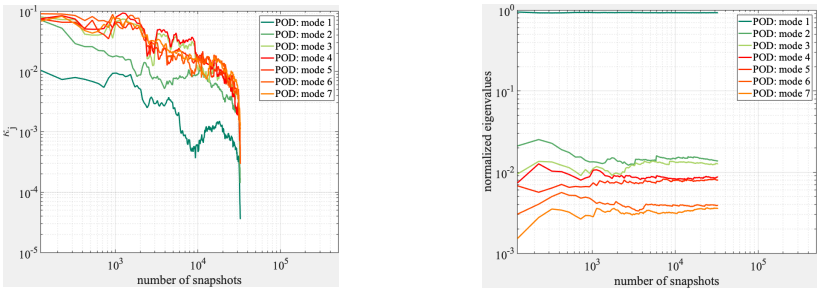

(a) Metric 1: POD eigenmodes

(b) Metric 2: normalized POD eigenvalues

Fig. 3. POD convergence results: (a) metric 1 and (b) metric 2.

wind-structure interaction standpoint, this implies the existence of physical correlation between projected modes, that is, similar POD modes may correspond to the same aerodynamic mechanism (Kim et al. 2018).

DMD Results

Similarly, convergence results of DMD analysis are summarized in Fig. 4. It should be observed that neither DMD modes nor the normalized DMD eigenvalues reach converge. This is caused by the DMD algorithm, where dynamic evolution is described by a pair of time-shifted matrices (Schmid 2010; Rowley et al. 2009; Chen et al. 2012). When the matrices are relatively small, that is, they only contain a few snapshots, DMD tends to produce a vastly expanded frequency band, where the amplitude spectra covers more isolated frequencies. When snapshots are increased, the observed frequencies of identified DMD modes cluster themselves in a narrower band. This is due to the degree of richness of aerodynamics increases when more snapshots are utilized. With a fixed number of extracted modes, aerodynamic patterns with similar features and distributions tend to cluster, and hence make their belonging cluster stand out and to be extracted as a mode. Thus, the observed frequencies may overlap with each other and may invalidate the adopted evaluation metrics (Muld et al. 2012b; Muld et al. 2012a).

Convergence of the frequency band To further investigate the aforementioned clustering properties, DMD is performed using a different number of snapshots. In Fig. 5, it can be seen that the frequency band shrinks rapidly when N_{snap} : 300 $\rightarrow$ 500 $\rightarrow$ 700. In particular, DMD modes

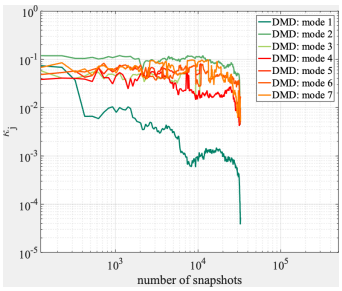

(a) Metric 1: DMD eigenmodes

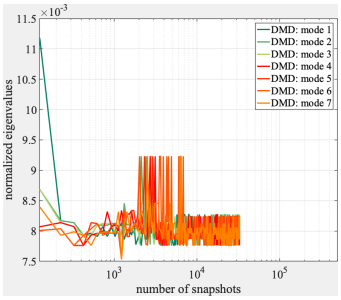

(b) Metric 2: normalized DMD eigenvalues

Fig. 4. DMD convergence results: (a) metric 1 and (b) metric 2.

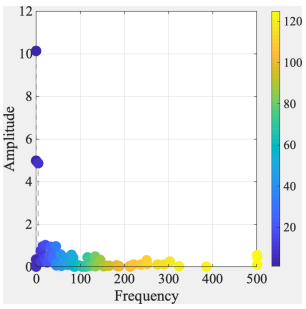

(a) X: 300 snapshots

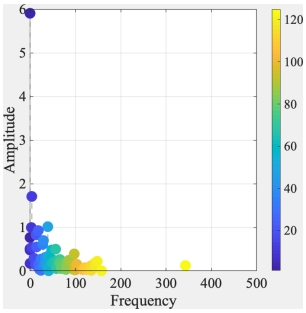

(b) X: 500 snapshots

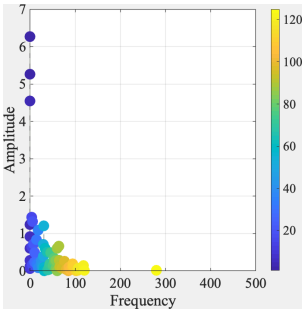

(c) X: 700 snapshots

Fig. 5. Convergence of the DMD frequency bands.

are sparsely scattered throughout the interval $[0, 500]$ when $N_{snap} = 300$ while the majority of resolved DMD modes are narrowed within a smaller interval $[0, 100]$ when $N_{snap} = 700$, indicating some DMD modes resemble each other when N_{snap} is large enough. Later in Section. 6, we will show that these modes share a global pattern in terms of explaining fluctuating wind pressures as well as providing different interpretations at a local scale, which are a reflection of the small scale turbulence features (Vickery 1966; Lee 1975; Cermak 1976). Therefore, DMD shows convergence in the context of the frequency band rather than the convergence of eigenvalues and eigenmodes in POD.

High/Low frequency dynamics Following the converged frequency bands results, the DMD energy spectrum with $N_{snap} = 800, 900$, and 1000 are examined. Frequencies have been normalized here using prism geometric parameter B and hourly average wind speed U for illustrative purposes.

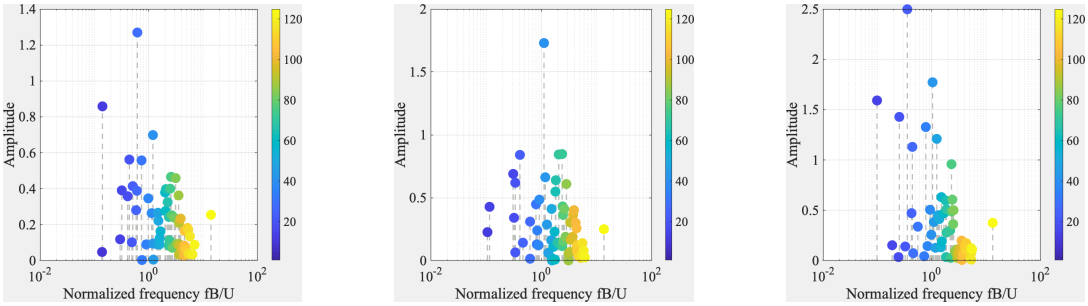

(a) X: 800 snapshots (b) X: 900 snapshots (c) X: 1000 snapshots

Fig. 6. Illustration of the dynamics in the converged frequency band.

The computed results confirm the convergence of the frequency band. In Fig. 6, the low-frequency region (blue dots) exhibits more distribution variation while the high-frequency region (yellow dots) is more unified and consistent with the change in N_{snap}. This observation supports other studies dealing with low frequency, large scale coherent structures, and cascading (Leonard 1975; Sirovich 1987; Holmes et al. 2012). Note each dot has a corresponding spatial pattern, and it is affected by a multitude of eddies of different sizes and strengths. Moreover, each mode is the representative of spatial patterns of a cluster. Therefore, decomposition results vary from case to case considering the richness and complexity of dynamics and the effects of snapshots on clustering results.

PART 2: SUFFICIENCY ANALYSIS RESULTS

Sufficiency of the POD eigenvalues

According to the convergence study results, the use of 1000 successive snapshots is able to produce well-converged POD modes (See Fig. 3). Thus, we performed the POD analysis using 1000 snapshots. Fig. 7 shows the sufficiency analysis results. The ratio of the cumulative sum of the POD eigenvalues is presented, where each eigenvalue is normalized by the total energy summation. The red stem extends from the baseline x-axis in Fig. 7 (a) shows the first eigenvalue ranked by the magnitude captures more than 90 percent of the energy. In many other studies, it was found that the first resolved POD mode is similar to the mean pressure distribution at different locations (Kareem and Cermak 1984; Tamura et al. 1999; Chen and Kareem 2005b; Carassale and Brunenghi 2011). To further investigate the aerodynamic fluctuation effects, the mean part

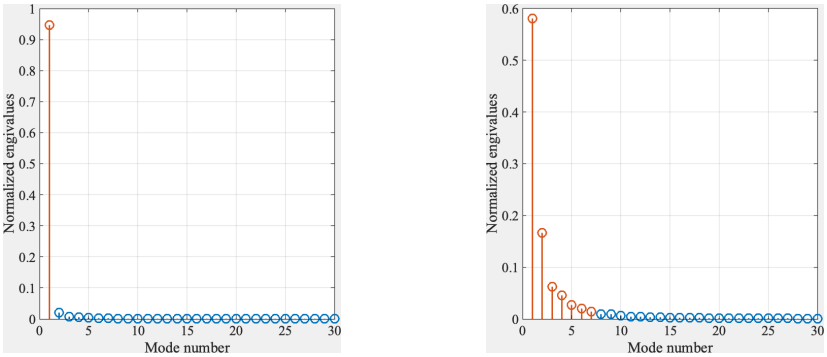

(a) Original dataset $\mathcal{D}$ (b) Mean value extracted dataset $\mathcal{D} - \bar{\mathcal{D}}$

Fig. 7. Cumulative eigenvalues versus the number of POD modes.

was extracted $\mathcal{D} - \bar{\mathcal{D}}$ and POD was applied to the fluctuation data. In Fig. 7 (b), it can be observed that 7 POD modes are needed to reconstruct 90 percent the dataset from an energetic perspective. Similarly, a need for more POD modes is identified in the other three faces. Compared to the windward face case, a more obvious exponential decay pattern is detected. The systematic examination results are available as supplementary material at the link. The difference reveals that the intrinsic complexity of the aerodynamic pressure field on the prism surface is related to the incoming turbulence. Specifically, the turbulence intensity is usually defined as the ratio of the root-mean-square (RMS) of the fluctuating wind velocity to the mean wind speed. The richness of fluctuating wind pressure dynamics presented in Fig. 7 (b) reflects the structure of incoming turbulence, which comes from a wide range of scales (Vickery 1966; Lee 1975; Cermak 1976).

Sufficiency of the delay-embedding and DMD eigenvalues

Stated in Eq. 14, we augmented the data by means of Takens embedding. In practice, a reasonable choice of embedding parameter delay step τ and embedding dimension d is critical as they both directly affect the accuracy of the embedded representation. First, the so-called average mutual information (AMI) that computes the dependence between two states $\boldsymbol{x}_k$ and $\boldsymbol{x}_{k+\tau}$ is adopted to determine τ. Specifically, Grassberger-Procaccia algorithm is used here to compute AMI (Grassberger and Procaccia 2004). Second, the method of false nearest neighbors (FNN), which identifies the nearest neighbor of a point is false if these two points are close only when

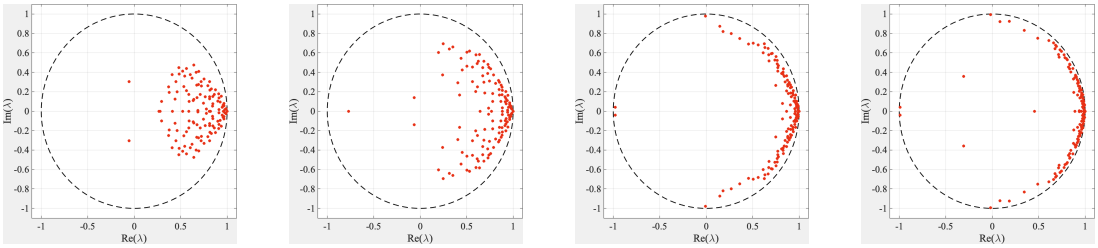

(a) Embedding number $i = 1$ (b) Embedding number $i = 2$ (c) Embedding number $i = 4$ (d) Embedding number $i = 8$

Fig. 8. Scatterplot of the DMD eigenvalues $\lambda_1, \ldots, \lambda_{125}$.

projected to a higher dimension, is implemented to estimate the minimally sufficient embedding number (Kennel et al. 1992). Fig. 8 shows the distribution of the computed DMD eigenvalues with a different embedding number. Eigenvalues are found to be unstable if their complex modulus is greater than 1 (i.e., are located outside the unit circle). Otherwise, eigenvalues are deemed as stable or neutrally stable (i.e., are located inside or on the unit circle) (Dawson et al. 2016). It can be seen that eigenvalues are gradually pushed to the circle boundary when the embedding number $i : 1 \rightarrow 2 \rightarrow 4 \rightarrow 8$. In this analysis, delay step τ is fixed to $3\Delta t$ and embedding number d is set to 17 for the windward data.

Similar to the POD sufficiency analysis (See Section. 5), we rank the complex-valued DMD eigenvalues by real part in descending order and plot the cumulative sum of DMD eigenvalues. The results are summarized in Fig. 9 and several properties are worth noting. First, the red line representing the complex modulus summation pattern gradually converges to diagonal reference line when the embedding number increases. The reference line is a simple linear function with zero intercepts and the slope is determined by the truncation number i, i.e. $y = 1/125x$. Unlike POD results, rapid growth of the cumulative eigenvalues is undetected in ordered DMD results (See the blue lines in Fig. 9). This is due to the fact that the fluctuating wind pressure of interest is spanned by an infinite Koopman modes. It is, therefore, the energy of the computed Koopman modes asymptotically converges to a uniform distribution and the cumulative summation becomes linear (Taira et al. 2017; Budišić et al. 2012; Arbabi and Mezic 2017). Second, both real and imaginary lines appear to be smoother when i becomes large, affirming the augmentation effects

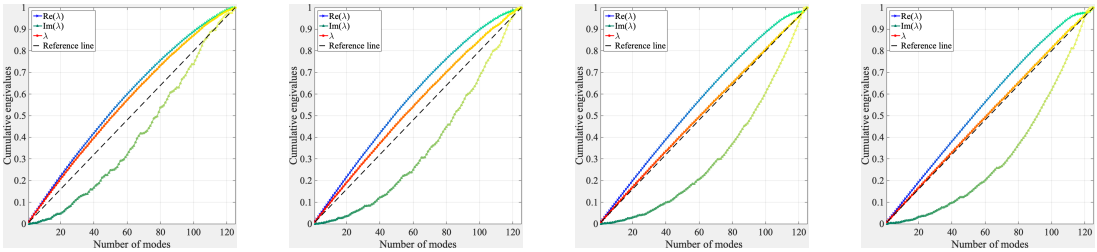

(a) Embedding number $i = 1$ (b) Embedding number $i = 2$ (c) Embedding number $i = 4$ (d) Embedding number $i = 8$

Fig. 9. Cumulative sum of eigenvalues versus the number of DMD modes. The straight reference line is a linear function whose independent variable is the number of DMD modes, the dependent variable is the normalized cumulative eigenvalues, and the intercept is 0.

brought by the delay coordinates. Third, the green line that covers the imaginary information of DMD eigenvalues is a downward convex function. Subsequently, the gradients of this function correspond to the phase information. It can be seen that the identified DMD modes with larger energy content tend to evolve at a slower pace than the low energy modes. This is similar to the turbulence where large eddies break into small eddies, which grow at a relatively higher range of frequencies (Lin et al. 2005; Leonard 1975; Tennekes et al. 1972; Majda and Lee 2014).

PART 3: ANALYSIS OF MODAL RESULTS

POD modes

First, we summarize the mean, variance, skewness, and kurtosis of the fluctuating wind pressures to show the connection between POD modes and statistical moments (See Fig. 10. (A)). It can be seen that the first POD mode is very similar to the mean and the variance that may be generally accessed via combining a set of POD modes (Tamura et al. 1999; Baker 2000; Carassale 2012). However, variability properties included in the skewness and kurtosis cannot be explained using the first four POD modes. This is caused by the POD algorithm, which by definition relies on the second-order statistical information (Chen and Kareem 2005b; Solari et al. 2007). Furthermore, POD modes (See Fig. 10. (B)) are usually assumed to be related to the energy distribution of random pressure fields (Lee 1975; Kim et al. 2018; Kareem and Cermak 1984; Solari et al. 2007). For instance, ϕ_1, ϕ_2, and ϕ_3 represent the pressure distributions that result in the along-wind overturning moment while ϕ_4 exhibits a pressure distribution pattern that is related to torsional

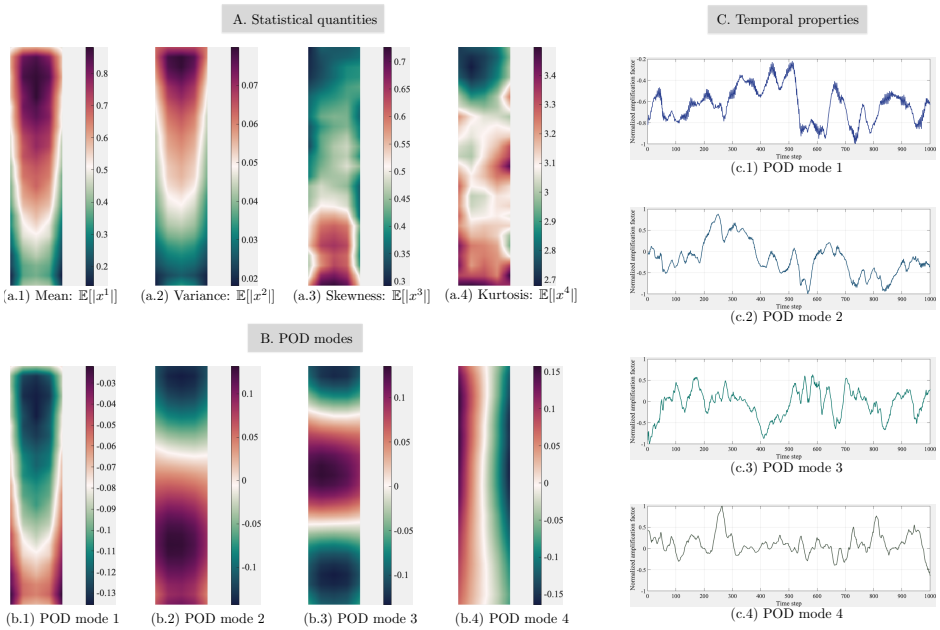

Fig. 10. Windward scenario: the decomposed spatial patterns and their time coefficients.

loads. Meanwhile, higher-order POD modes include more small scale features for analyzing localized effects. For example, peak values of ϕ_4 are found around the prism edges. Similar results have been observed in the leeward and two sidefaces where min-max values are around corners, suggesting the locations where large pressure fluctuations take place (Kim et al. 2018; Tamura et al. 1999; Carassale 2012). The time coefficients associated with the computed POD modes are presented in Fig. 10. (C). They are changing abruptly in time, precluding identification of qualitative description of aerodynamic characteristics. This is caused by the zero-time-lag covariance matrix used in the POD analysis (Taira et al. 2017; Towne et al. 2018; Zhao et al. 2019; Carassale 2012). Because such covariance matrix does not contain any evolution information, the decomposition results in assigning an eigenmode with multiple frequencies in such a way rely on the L_2 norm error in the POD formulation to be minimum (Chen and Kareem 2005b; Carassale 2012).

DMD modes

Clustering results To compute DMD modes, 730 snapshots are used with embedding number $i = 30$ and truncation number $r = 125$. Because the decomposition process generates 125

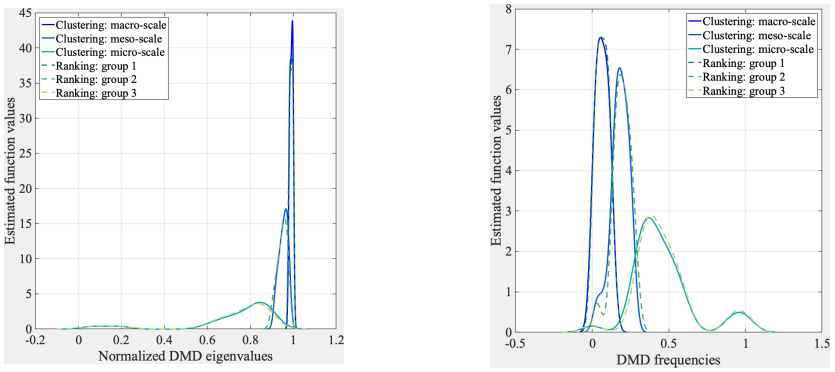

(a) Eigenvalue distribution

(b) Frequency distribution

Fig. 11. Distributions of clustered eigenvalues and frequencies.

eigenmodes, a clustering method, as well as a physical grouping method, are adopted to group DMD modes of similar properties. First, k-means clustering has been implemented out of a need to control the number of clusters (Arthur and Vassilvitskii 2007; Murphy 2012). Specifically, cluster number is set to 3, DMD modes have been normalized, and the distance metric involved in the cluster analysis is set as the correlation type. As a result, there are three types of DMD modes categorized by the scale of spatial patterns, i.e. macro-scale, meso- scale, and micro-scale. Second, we rank DMD modes by the real part of the eigenvalue in descending order and classify them into three groups, where group 1 is $\{\phi_1, \ldots, \phi_{42}\}$, group 2 is $\{\phi_{43}, \ldots, \phi_{84}\}$, and group 3 is $\{\phi_{85}, \ldots, \phi_{125}\}$. Subsequently, we approximate the distribution of DMD eigenvalues and frequencies associated with each cluster/group utilizing a normal kernel smoothing function. In Fig. 11, it can be observed that the clustering and physical grouping results are highly similar. In particular, macro-scale DMD modes tend to have larger eigenvalues while the normalized eigenvalues of micro-scale DMD modes spread over the entire interval. Such finding indicates macro-scale DMD modes contain more energy. In light of the oscillation frequency, macro-scale DMD modes have a relatively lower frequency range compared to the other two types. This observation is similar to turbulence at different length scales, where frequencies of large eddies are much smaller than small eddies (Holmes et al. 2012; Tennekes et al. 1972).

Energy cascade The clustering results indicate there exists a link reflecting cascading in the

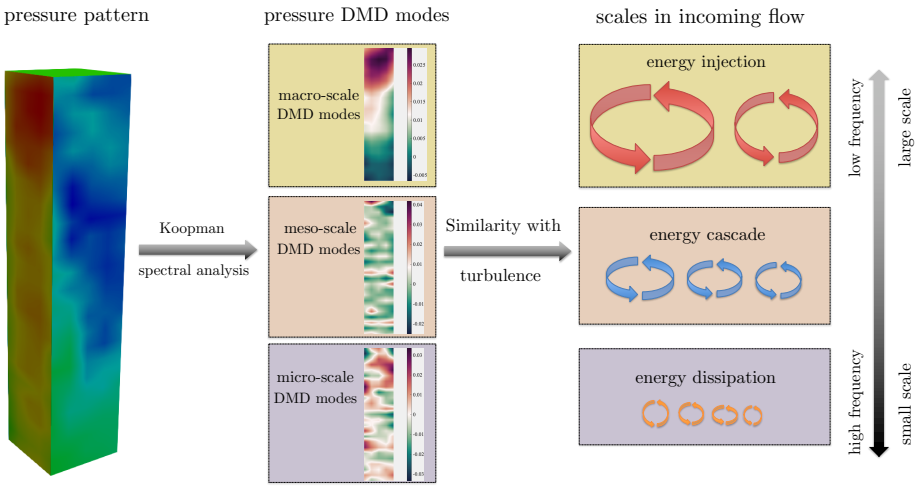

Fig. 12. Similarities of clustered DMD modes at different scales with turbulence energy distribution.

pressure field akin to a typical turbulence field. It is known that the aerodynamic fluctuating loads acting on the windward face of the prism model are dominated by the approach flow turbulence (Chen and Kareem 2004; Cermak 1976; Tanaka et al. 2012; Chen 2013). Meanwhile, aerodynamic loads acting on the two side and leeward faces are closely related to the wake dynamics including vortex shedding, which in turn is influenced by the turbulence in the approach flow (Vickery 1966; Lee 1975; Kareem and Cermak 1984; Aubry et al. 1988). These experimental findings show the cascading features in the aerodynamic pressure represented by combining the DMD modes and their time coefficients. To understand how cascading relates to the aerodynamics pressure field around prisms, we focus on explaining the energy transfer by investigating the dynamical evolution of each DMD mode. In particular, the dynamical evolution process is similar to the energy transferring mechanism in turbulence, which includes energy cascade, neutrally steady, and inverse cascade (Leonard 1975; Majda and Lee 2014). Furthermore, it should be noted that the spatial patterns in the pressure field are similar to the distribution of length scales (eddy sizes) in the incoming turbulent flow. Fig. 12 schematically highlights these observations, where macro-, meso-, and micro-scale pressure fluctuations mimic turbulence cascade through energy injection, cascade, and dissipation respectively.

Examination of the spatial distribution POD is useful to study eigenmodes of the pressure

fluctuations on the surface of a prism. Here, DMD is applied to further investigate the spatiotemporal variation of the pressure fields and to understand potential discrepancies in POD and DMD.

Overall, spatial coherence embedded in the extracted DMD modes decrease gradually from the macro-scale to the meso-scale group and finally cascade to the micro-scale group. For each group, two modes are randomly selected to demonstrate such cascading and are presented in Fig. 13. It can be observed that the macro-scale DMD modes are similar to the most energetic POD modes. They provide a global footprint of the aerodynamic pressure by reflecting the overall distribution of the fluctuating pressures acting on the prismatic model. For instance, the two selected macro modes are evaluated at normalized frequencies 0.0165 and 0.1225 respectively from top to bottom in Fig. 13. The mode associated with the smaller frequency is more predominant spatiotemporally compared to the other mode. In particular, the top macro-scale DMD mode shown in Fig. 13 is in good agreement with the force pattern representing the overturning moment. Meanwhile, locations of local minima and maxima of a macro-scale DMD mode serve as scaled features of overturning forces. The distinct separation of minimum and maximum values further emphasizes macro-scale DMD modes echo the overall overturning moment on the windward surface. Very similar results have been found in the POD modes (Kim et al. 2018; Kareem and Cermak 1984; Tamura et al. 1999; Carassale and Brunenghi 2011).

Meanwhile, the amplitudes of DMD modes are determined by the real part of the computed DMD eigenvalues and the frequencies are determined by the imaginary part. The distribution of DMD eigenvalues on the unit circle shown in Fig. 13 indicate macro-scale DMD modes are more energetic than other types of modes. They are connected to large scale flow features. Therefore, they relate to energy injected by the approach flow and represent its spatiotemporal features (Carassale 2012). In the following analysis of their temporal evolution (See Fig. 14), it is at the dominant vortex shedding frequency resulting in a snapshot of a large scale structure convecting over the side face. Unlike the pressure field on a 2D prism, a finite height prism in a shear flow experiences vortex shedding at slightly different frequencies in cells of finite length along the height. Accordingly, DMD modes of pressure fluctuations associated with finite height prisms in shear flows would

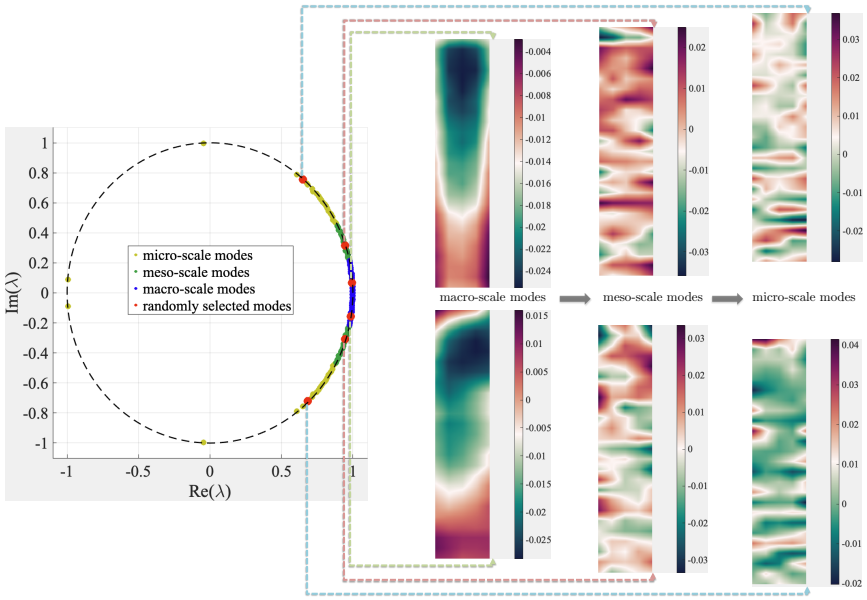

Fig. 13. Spatial patterns of computed DMD modes of the windward.

reflect spatially less correlated patterns.

For the micro-scale DMD modes, small eddies, in a generic sense, represent the instabilities of local interactions between different fluid motions. According to the Kolmogorov length scale theory (Frisch and Kolmogorov 1995), small eddies tend to have high frequencies, causing turbulence to be isotropic and homogeneous at a local scale. The micro-scale DMD modes shown in 13 from the windward case to illustrate such pressure fluctuations. It should be noted that peak values in most micro-scale DMD modes are randomly distributed. These peak value areas are relatively small and sparsely scattered. This observation conforms to the characteristics of small eddies (randomness and size) (Tennekes et al. 1972; Frisch and Kolmogorov 1995).

In (Baker 2000), it was pointed that the least energetic modes may contain information on the interaction between different mechanisms instead of representing a specific one. The conclusion was drawn based on POD results, where the temporal behavior of identified eigenmodes is hard to interpret. Using Eq. 6, one can find the selected micro-scale DMD modes decay with time. The amplitude distribution shown in Fig. 13 suggest some of the micro-scale modes decays exponentially. This suggests that the kinetic energy carried by small scales ultimately dissipates.

Examination of the temporal evolution As wind passes by a building, it results in the formation

of Karman vortex shedding in its wake. It is pointed out earlier that for prisms exposed to a shear/boundary layer flow the vortex shedding frequency is not uniform along the height and occurs in cells of finite length. As these vortices are advected by the mean flow which varies with height, they result in interactive periodic pressure signatures on the building side faces (Lee 1975). Few studies have been reported that connect identified eigenmodes to the convection of the vortices (vortex tubes) because of the spatiotemporal nature of these recurrent patterns. In (Carassale 2012), the effects of the advection of vortices on the pressure patterns have been identified by repeated operations of the digital filter and Hilbert transform of the convolutive data. In this context, DMD utilizes a paired time-shifted matrices in the computation of eigenmodes, which naturally integrates the evolution dynamics into the decomposition process. In addition, the delaying coordinates used in this study serve as an alternative representation to the convolution operation for dynamical PCA/ICA model adopted in (Carassale 2012). Fig. 14 shows the temporal evolution of the pressure field via dynamic modes at different scales. The time between snapshots equals the sampling period of the measured data $10\Delta t$, $5\Delta t$, and Δt for the macro-, meso-, and micro-scale modes respectively. A total length of 7 sequences are presented. The macro-scale sequences reported in Fig. 14 (a) shows a propagation of the topology of a vortex tube on the side face as it advects along the width of the face that are associated with the vortex shedding frequency. While in Fig. 14 (b) at the meso-scale the evolution of limited vortex structures that emerge due to shear in the approach flow, as noted earlier, is found. Also near the base there appears to be a collection of a horseshoe vortex-like features. A more in-depth analysis is needed to examine their features. At the micro-scale, depending on the selected frequency, one can observe organized small scale features being convected along the side. Similar observations were noted in (Carassale 2012) though the analysis was carried out in a band of frequencies rather than individual frequencies permitted by DMD analysis. The results affirm that the spatialtemporal evolution of DMD modes at different scales can capture the characteristic features of the overall pressure dynamics. Whereas at lower frequencies, macro-scale DMD modes serve as the foundation of the aerodynamic pressure field from the energy perspective and meso/micro modes present portraits of more localized fluctuations

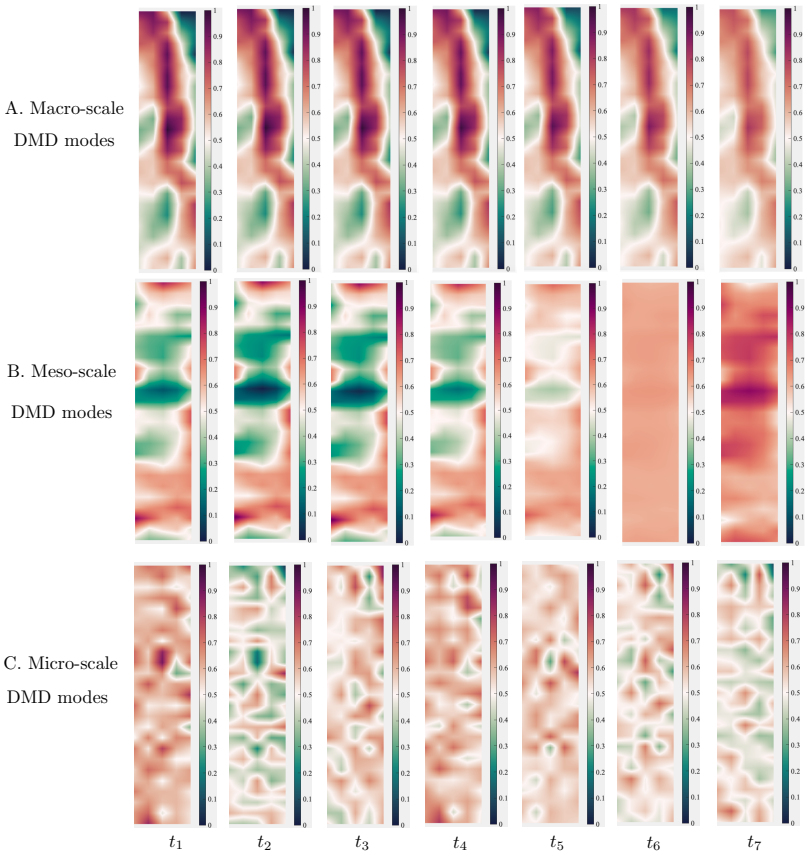

Fig. 14. Temporal evolution of selected DMD modes of the leftside.

with relatively higher frequencies and smaller spatial scales.

Stripe pattern A specific micro-scale pattern that is detected on all surfaces of the prism is noteworthy. Based on the appearance we refer it as the stripe pattern because the computed spatial distribution indicates the surface is divided into a few bands. Pressures at two adjacent bands come from different amplitudes, thus resembles the stripe pattern observed in nature. To understand these stripe patterns, we examined the evolution of the pressure distribution, finding such micro-scale pattern to be closely related to the pressure increment between instantaneous spatial pressure distribution. Fig. 15, the first row shows the pressure distribution at two consecutive time instances t_1 and t_2 as well as the instantaneous pressure increment between $p(t_1)$ and $p(t_2)$. The second row displays the identified stripe pattern observed in DMD modes. Fluctuating pressure scales of different sizes have their corresponding position in a frequency spectrum. In Fig. 15, size of

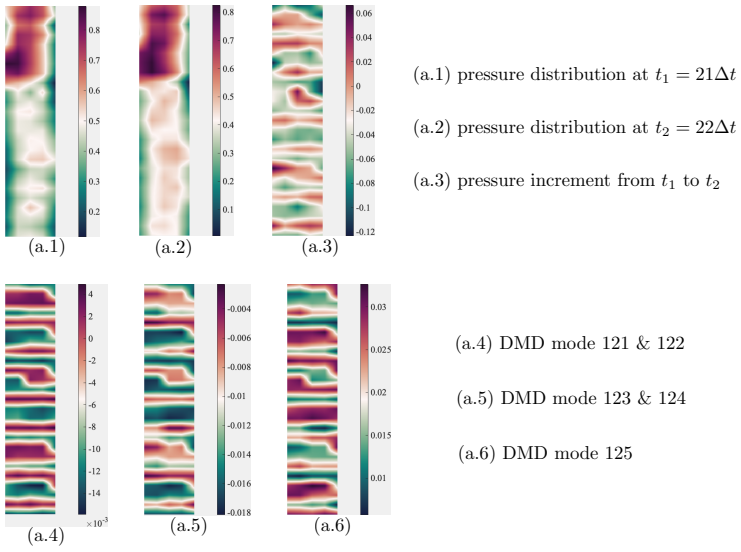

Fig. 15. Illustration of the connection between micro-scale DMD modes and instantaneous increment of wind pressures.

the stripe patterns are structurally similar, indicating the size and frequency of the surrounding fluctuations are very close.

These factors naturally fulfill the precondition of the beating phenomenon in a coupled system, which in principle is a constructive interference between two signal having almost identical frequencies (Yalla and Kareem 2001). The decomposition results describing the dynamical evolution of each stripe pattern mode are given in Fig. 16. The identified DMD modes oscillate and the envelope amplitudes essentially exhibit a decaying pattern. This is due to the fact that small scales are gradually damped. Moreover, the beat phenomenon that is highlighted by the red dots only happens in the high-frequency region (See Fig. 16). An intuitive explanation is based on the definition of the beating phenomenon, which not only requires the existence of two fluid pressure regions sharing very close frequencies but also expects these to be closely spaced to be interactive. On the other hand, large scale fluctuations associated with larger-scale motions do not see such as beating phenomenon.

Description in discrete Fourier domain In (Chen et al. 2012), it was pointed out that DMD provides identical results to the temporal discrete Fourier transform (DFT) if the input data is

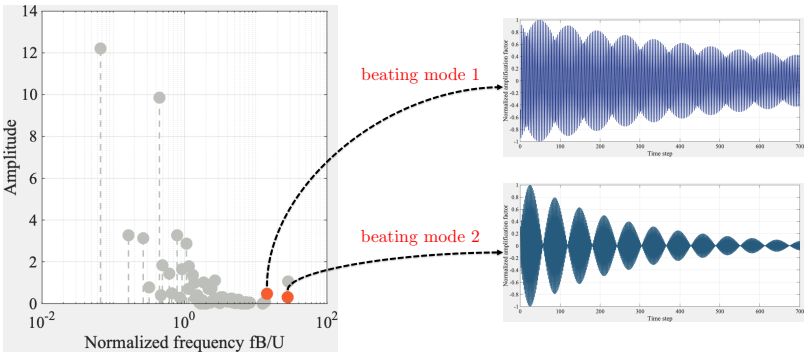

Fig. 16. Properties of the stripe pattern.

linearly independent and zero centered (Chen et al. 2012). Despite the fact that our aerodynamic pressure data is highly nonlinear and the mean is not subtracted, DMD spectrum was found to provide useful information regarding the pressure dynamics from the frequency perspective (Tu et al. 2013; Kutz et al. 2016). In this context, the mode amplitude was modeled as a function of frequency, which can be computed from the imaginary part of the DMD eigenvalues. Such spectrum captures the magnitude and phase of pressure dynamics through a linear combination of eigenvectors, where every eigenvector grows or decays at a specified frequency according to its associated eigenvalue. For comparison, we computed the amplitude of oscillations at a wide range of frequencies by means of the Fourier transform, where the temporal DFT is essentially a portrait of the energy of a series of harmonic oscillators (Fig. 17 (a)). Whereas Fig. 17 (b) shows that the DMD spectrum resembles the FFT spectrum, where the leading components of the power spectrum computed by the FFT are captured by DMD. The difference between the DMD and FFT spectra comes from the nature of the analysis. In particular, FFT spectrum is computed independently using the collected time series data recorded at each pressure tap, that is, it returns 125 Fourier-transformed vectors. The mean of this multidimensional array is calculated and presented by the red line in Fig. 17 (a). On the other hand, every single component in the DMD spectrum represents a certain coherent structure enveloping 125 pressure taps over each surface.

CONCLUDING REMARKS

This study investigates the dynamics of random pressure fields over bluff bodies with an

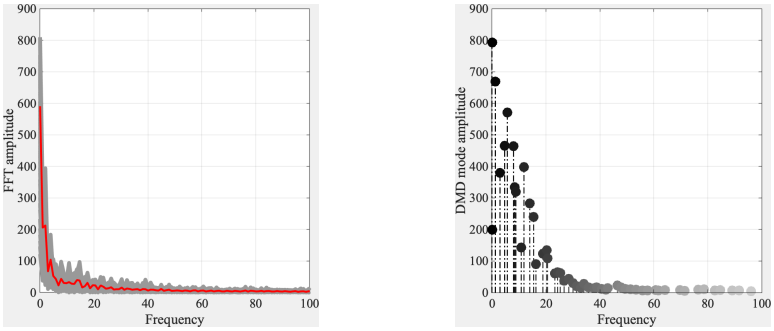

(a) FFT spectrum (b) DMD spectrum

Fig. 17. DFT and DMD spectrum. In the DFT spectrum representations, the gray band represent the discrete Fourier transform (DFT) results of 125 time-ordered sequences and the red line denotes their mean.

application to surface pressure on a prism immersed in a turbulent boundary layer. An operator-theoretic approach is considered for the aerodynamic characterization using limited wind tunnel test data. First, the nonlinear pressure dynamics is linearized in the entire basin by an infinite-dimensional linear operator, i.e. the Koopman operator. Subsequently, spectral analysis of the Koopman operator provides a spatiotemporal characterization of the pressure data. To compute the Koopman eigen-elements, dynamic mode decomposition is performed using time delay coordinates. As a result, the computed DMD representation is spatiotemporally orthogonal where each identified flow structure is assigned to a specific frequency and a corresponding temporal growth/decay.

A comparative study between POD and DMD is carried out. Unlike POD, which tends to mix the temporal frequencies in the identified modes, DMD provides single-frequency eigenmodes. The macro-scale modes can identify the pattern of vortices (or vortex tubes) shed from the upstream edge of the side face, whereas other aerodynamic features are captured at the meso and micro scales. It is also noted that DMD modes mirror the characteristics of turbulence approaching the prism. Specifically, akin to turbulence cascade, the macro-scale DMD modes break up cascading down to micro-scale that represents the instantaneous pressure increments and small eddy dynamics.

Future directions regarding applying the Koopman operator to learn similar nonlinear dynamical systems include: (1) Extension of the current work to the extreme learning condition where available

data is merely a sequence of a scalar, (2) Development of an efficient computation framework for applying the Koopman operator to streaming datasets, and (3) Moving from the current Laplacian determinism to learning the intrinsic order in chaotic systems.

ACKNOWLEDGMENTS

This work was supported in part by the National Science Foundation (NSF) under Grant No. 1562244. This support is gratefully acknowledged. The authors also acknowledge gratefully the use of Tokyo Polytechnic University aerodynamic database.

DATA AVAILABILITY STATEMENT

Some or all data, models, or code generated or used during the study are available in a repository online (https://xihaier.github.io/) in accordance with funder data retention policies.

APPENDIX. ILLUSTRATION EXAMPLE

In this appendix, a synthetic dataset with two hyperbolic oscillations is created for testing the performance of different decomposition methods (Kutz et al. 2016). The DMD results are compared against the results obtained using the POD and independent component analysis (ICA) method. The spatial modes take the following formula:

$$\begin{aligned} u_1 &= \exp(-((x+10)^2 + (y+10)^2)/100) \\ u_2 &= \exp(-((x-10)^2 + (y-10)^2)/100) \end{aligned} \tag{15}$$

Specifically, the spatial domain $\Omega \subset [-30, 30] \times [-30, 30]$ with 70 elements per axis, resulting in a resolution of $70 \times 70 = 4900$ per snapshot. The first mode u_1 oscillates at $7Hz$ and the second mode u_2 oscillates at $3Hz$. Note both modes are stationarily oscillate for the entire during of the simulation. The data is recorded with $\delta t = 0.01$ and a total of 1000 snapshots have been collected for analysis. Fig. 18 shows the states of the first 10 equispaced time instances. Apparently, two modes have overlapped spatial distributions and they are evolving at different frequencies. To accelerate the decomposition process, the method of snapshot is considered for the implementation of DMD and POD (Schmid 2010; Chen et al. 2012; Tu et al. 2013), that is, the input matrix is

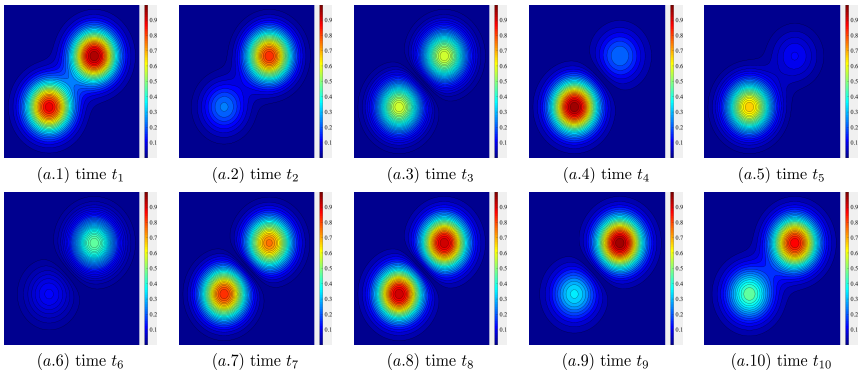

Fig. 18. Snapshots of the dynamical system.

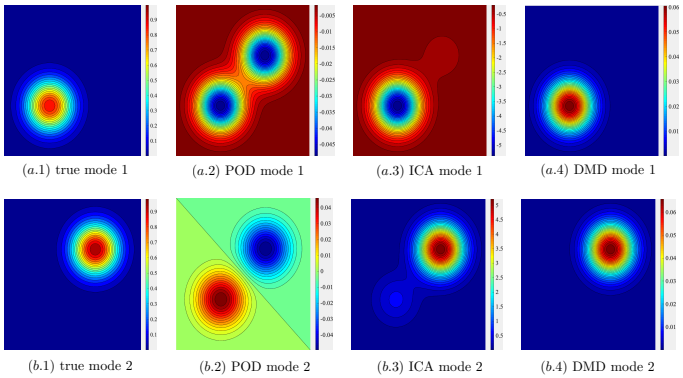

Fig. 19. Spatial decomposition results of 2D example.

reshaped into the size of $\mathcal{D} \in \mathbb{R}^{4900\times1000}$. Fig. 19 shows DMD accurately captures the distribution of true modes compared to the POD and ICA. Beyond that, the evolution provided by the DMD algorithm matches well with the true dynamics (See Fig. 20). In terms of POD, it focuses on finding the eigenmodes that are energetically optimal regarding the reconstruction of the input data. Hence, the POD modes are very similar to the spatial average results. ICA modes are more isolated and results become ambiguous around the overlapped area.

APPENDIX. EVALUATION METRICS FOR CONVERGENCE STUDY

We check the convergence of the decomposition results using both eigenmodes and eigenvalues (Muld et al. 2012b; Muld et al. 2012a). The first evaluation metric is a function of identified eigenmodes. It is used to analyze the convergence behavior of the spatial pattern. Consider two datasets $\mathcal{D}^1 = \{\boldsymbol{x}(t_1), \ldots, \boldsymbol{x}(t_m)\}$ and $\mathcal{D}^2 = \{\boldsymbol{x}(t_1), \ldots, \boldsymbol{x}(t_n)\}$, which contain pressure signals

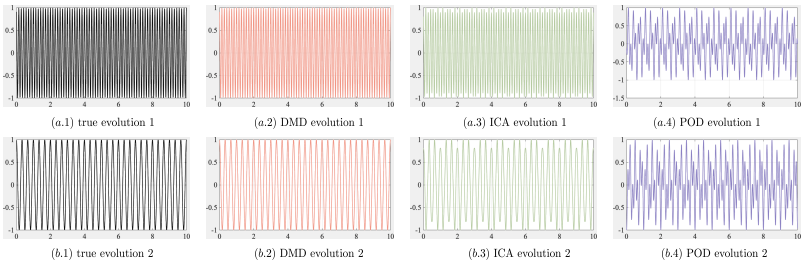

Fig. 20. Temporal decomposition results of 2D example.

of the same prism surface but with a different sampling interval $[t_1, t_m]$ and $[t_1, t_n]$. Two sets of eigenmodes $\mathbf{\Phi}^m$ and $\mathbf{\Phi}^n$ can be accordingly computed by means of either POD or DMD method. To measure their relative difference, a L_2 norm based metric is defined:

$$\kappa_j =< \phi_j^m - \phi_j^n, \phi_j^m - \phi_j^n >_{\Omega_x} \tag{16}$$

In this study, $n = 30000$, serving as the reference point in investigating convergence properties, and m is sampled from the interval $[\Delta t, n\Delta t]$.

Meanwhile, the second evaluation metric is a function defined based on the normalized eigenvalues:

$$\lambda_j^{\dagger} = \frac{\lambda_j}{\sum_{i=1}^{n} \lambda_i \, (m)} \tag{17}$$

where $\lambda_j^{\dagger}$ primarily examines the temporal convergence properties. It should be further noted that the DMD eigenvalues λ_j^{DMD} and eigenmodes ϕ_j^{DMD} are complex-valued. For this reason, complex modulus that measures the magnitude of a tensor from the coordination center to its location in the complex plane is utilized:

$$\begin{aligned} \lambda_j^{DMD} &= \sqrt{\left(\mathcal{R}e\left(\lambda_j^{DMD}\right)\right)^2 + \left(\mathcal{I}m\left(\lambda_j^{DMD}\right)\right)^2} \\ \phi_j^{DMD} &= \sqrt{\left(\mathcal{R}e\left(\phi_j^{DMD}\right)\right)^2 + \left(\mathcal{I}m\left(\phi_j^{DMD}\right)\right)^2} \end{aligned} \tag{18}$$

REFERENCES

"Tpu aerodynamic database: Wind pressure database based on wind tunnel experiment for high-rise building (http://wind.arch.t-kougei.ac.jp/system/eng/contents/code/tpu).

Arbabi, H. and Mezic, I. (2017). "Ergodic theory, dynamic mode decomposition, and computation of spectral properties of the koopman operator." *SIAM Journal on Applied Dynamical Systems*, 16(4), 2096–2126.

Arthur, D. and Vassilvitskii, S. (2007). "k-means++: The advantages of careful seeding." *Proceedings of the eighteenth annual ACM-SIAM symposium on Discrete algorithms*, Society for Industrial and Applied Mathematics, 1027–1035.

Aubry, N., Holmes, P., Lumley, J. L., and Stone, E. (1988). "The dynamics of coherent structures in the wall region of a turbulent boundary layer." *Journal of Fluid Mechanics*, 192, 115–173.

Baker, C. (2000). "Aspects of the use of proper orthogonal decomposition of surface pressure fields." *Wind and Structures*, 3(2), 97–115.

Berkooz, G., Holmes, P., and Lumley, J. L. (1993). "The proper orthogonal decomposition in the analysis of turbulent flows." *Annual review of fluid mechanics*, 25(1), 539–575.

Bistrian, D. A. and Navon, I. M. (2015). "An improved algorithm for the shallow water equations model reduction: Dynamic mode decomposition vs pod." *International Journal for Numerical Methods in Fluids*, 78(9), 552–580.

Brunton, S. L., Brunton, B. W., Proctor, J. L., Kaiser, E., and Kutz, J. N. (2017). "Chaos as an intermittently forced linear system." *Nature communications*, 8(1), 1–9.

Budišić, M., Mohr, R., and Mezić, I. (2012). "Applied koopmanism." *Chaos: An Interdisciplinary Journal of Nonlinear Science*, 22(4), 047510.

Carassale, L. (2012). "Analysis of aerodynamic pressure measurements by dynamic coherent structures." *Probabilistic engineering mechanics*, 28, 66–74.

Carassale, L. and Brunenghi, M. M. (2011). "Statistical analysis of wind-induced pressure fields: A methodological perspective." *Journal of Wind Engineering and Industrial Aerodynamics*, 99(6-7), 700–710.

Carassale, L., Piccardo, G., and Solari, G. (2001). "Double modal transformation and wind engi-

neering applications." *Journal of engineering mechanics*, 127(5), 432–439.

Carassale, L. and Solari, G. (2002). "Wind modes for structural dynamics: a continuous approach." *Probabilistic Engineering Mechanics*, 17(2), 157–166.

Cermak, J. (1976). "Aerodynamics of buildings." *Annual Review of Fluid Mechanics*, 8(1), 75–106.

Chen, K. K., Tu, J. H., and Rowley, C. W. (2012). "Variants of dynamic mode decomposition: boundary condition, koopman, and fourier analyses." *Journal of nonlinear science*, 22(6), 887–915.

Chen, X. (2013). "Estimation of stochastic crosswind response of wind-excited tall buildings with nonlinear aerodynamic damping." *Engineering structures*, 56, 766–778.

Chen, X. and Kareem, A. (2004). "Equivalent static wind loads on buildings: New model." *Journal of Structural Engineering*, 130(10), 1425–1435.

Chen, X. and Kareem, A. (2005a). "Coupled dynamic analysis and equivalent static wind loads on buildings with three-dimensional modes." *Journal of structural Engineering*, 131(7), 1071–1082.

Chen, X. and Kareem, A. (2005b). "Proper orthogonal decomposition-based modeling, analysis, and simulation of dynamic wind load effects on structures." *Journal of Engineering Mechanics*, 131(4), 325–339.

Cui, W. and Caracoglia, L. (2018). "A fully-coupled generalized model for multi-directional wind loads on tall buildings: A development of the quasi-steady theory." *Journal of Fluids and Structures*, 78, 52–68.

Dawson, S. T., Hemati, M. S., Williams, M. O., and Rowley, C. W. (2016). "Characterizing and correcting for the effect of sensor noise in the dynamic mode decomposition." *Experiments in Fluids*, 57(3), 42.

Ding, F., Kareem, A., and Wan, J. (2019). "Aerodynamic tailoring of structures using computational fluid dynamics." *Structural Engineering International*, 29(1), 26–39.

Frisch, U. and Kolmogorov, A. N. (1995). *Turbulence: the legacy of AN Kolmogorov*. Cambridge university press.

Giannakis, D. (2019). "Data-driven spectral decomposition and forecasting of ergodic dynamical

systems." *Applied and Computational Harmonic Analysis*, 47(2), 338–396.

Grassberger, P. and Procaccia, I. (2004). "Measuring the strangeness of strange attractors." *The Theory of Chaotic Attractors*, Springer, 170–189.

Holmes, P., Lumley, J. L., Berkooz, G., and Rowley, C. W. (2012). *Turbulence, coherent structures, dynamical systems and symmetry*. Cambridge university press.

Huang, G. and Chen, X. (2007). "Wind load effects and equivalent static wind loads of tall buildings based on synchronous pressure measurements." *Engineering Structures*, 29(10), 2641–2653.

Kareem, A. and Cermak, J. (1984). "Pressure fluctuations on a square building model in boundary-layer flows." *Journal of Wind Engineering and Industrial Aerodynamics*, 16(1), 17–41.

Kennel, M. B., Brown, R., and Abarbanel, H. D. (1992). "Determining embedding dimension for phase-space reconstruction using a geometrical construction." *Physical review A*, 45(6), 3403.

Kim, B., Tse, K., and Tamura, Y. (2018). "Pod analysis for aerodynamic characteristics of tall linked buildings." *Journal of Wind Engineering and Industrial Aerodynamics*, 181, 126–140.

Klus, S., Koltai, P., and Schütte, C. (2015). "On the numerical approximation of the perron-frobenius and koopman operator." *arXiv preprint arXiv:1512.05997*.

Koopman, B. O. (1931). "Hamiltonian systems and transformation in hilbert space." *Proceedings of the National Academy of Sciences of the United States of America*, 17(5), 315.

Kutz, J. N., Brunton, S. L., Brunton, B. W., and Proctor, J. L. (2016). *Dynamic mode decomposition: data-driven modeling of complex systems*. SIAM.

Le Clainche, S. and Vega, J. M. (2017). "Higher order dynamic mode decomposition." *SIAM Journal on Applied Dynamical Systems*, 16(2), 882–925.

Lee, B. (1975). "The effect of turbulence on the surface pressure field of a square prism." *Journal of Fluid Mechanics*, 69(2), 263–282.

Leonard, A. (1975). "Energy cascade in large-eddy simulations of turbulent fluid flows." *Advances in geophysics*, Vol. 18, Elsevier, 237–248.

Lin, N., Letchford, C., Tamura, Y., Liang, B., and Nakamura, O. (2005). "Characteristics of wind forces acting on tall buildings." *Journal of Wind Engineering and Industrial Aerodynamics*,

93(3), 217–242.

Lusch, B., Kutz, J. N., and Brunton, S. L. (2018). "Deep learning for universal linear embeddings of nonlinear dynamics." *Nature communications*, 9(1), 1–10.

Majda, A. J. and Lee, Y. (2014). "Conceptual dynamical models for turbulence." *Proceedings of the National Academy of Sciences*, 111(18), 6548–6553.

Mezić, I. (2005). "Spectral properties of dynamical systems, model reduction and decompositions." *Nonlinear Dynamics*, 41(1-3), 309–325.

Muld, T. W., Efraimsson, G., and Henningson, D. S. (2012a). "Flow structures around a high-speed train extracted using proper orthogonal decomposition and dynamic mode decomposition." *Computers & Fluids*, 57, 87–97.

Muld, T. W., Efraimsson, G., and Henningson, D. S. (2012b). "Mode decomposition on surface-mounted cube." *Flow, turbulence and combustion*, 88(3), 279–310.

Murphy, K. P. (2012). *Machine learning: a probabilistic perspective*. MIT press.

Rowley, C. W., Mezić, I., Bagheri, S., Schlatter, P., and Henningson, D. S. (2009). "Spectral analysis of nonlinear flows." *Journal of fluid mechanics*, 641, 115–127.

Schmid, P. J. (2010). "Dynamic mode decomposition of numerical and experimental data." *Journal of fluid mechanics*, 656, 5–28.

Sirovich, L. (1987). "Turbulence and the dynamics of coherent structures. i. coherent structures." *Quarterly of applied mathematics*, 45(3), 561–571.

Solari, G. (2016). "Thunderstorm response spectrum technique: theory and applications." *Engineering Structures*, 108, 28–46.

Solari, G., Carassale, L., and Tubino, F. (2007). "Proper orthogonal decomposition in wind engineering. part 1: A state-of-the-art and some prospects." *Wind and Structures*, 10(2), 153–176.

Taira, K., Brunton, S. L., Dawson, S. T., Rowley, C. W., Colonius, T., McKeon, B. J., Schmidt, O. T., Gordeyev, S., Theofilis, V., and Ukeiley, L. S. (2017). "Modal analysis of fluid flows: An overview." *AIAA Journal*, 4013–4041.

Takens, F. (1981). "Detecting strange attractors in turbulence." *Dynamical systems and turbulence,*

Warwick 1980, Springer, 366–381.

Tamura, Y., Suganuma, S., Kikuchi, H., and Hibi, K. (1999). "Proper orthogonal decomposition of random wind pressure field." *Journal of Fluids and Structures*, 13(7-8), 1069–1095.

Tanaka, H., Tamura, Y., Ohtake, K., Nakai, M., and Kim, Y. C. (2012). "Experimental investigation of aerodynamic forces and wind pressures acting on tall buildings with various unconventional configurations." *Journal of Wind Engineering and Industrial Aerodynamics*, 107, 179–191.

Tennekes, H., Lumley, J. L., Lumley, J., et al. (1972). *A first course in turbulence*. MIT press.

Towne, A., Schmidt, O. T., and Colonius, T. (2018). "Spectral proper orthogonal decomposition and its relationship to dynamic mode decomposition and resolvent analysis." *Journal of Fluid Mechanics*, 847, 821–867.

Tu, J. H., Rowley, C. W., Luchtenburg, D. M., Brunton, S. L., and Kutz, J. N. (2013). "On dynamic mode decomposition: theory and applications." *arXiv preprint arXiv:1312.0041*.

Vickery, B. (1966). "Fluctuating lift and drag on a long cylinder of square cross-section in a smooth and in a turbulent stream." *Journal of Fluid Mechanics*, 25(3), 481–494.

Williams, M. O., Kevrekidis, I. G., and Rowley, C. W. (2015). "A data–driven approximation of the koopman operator: Extending dynamic mode decomposition." *Journal of Nonlinear Science*, 25(6), 1307–1346.

Yalla, S. K. and Kareem, A. (2001). "Beat phenomenon in combined structure-liquid damper systems." *Engineering Structures*, 23(6), 622–630.

Zhang, Q., Liu, Y., and Wang, S. (2014). "The identification of coherent structures using proper orthogonal decomposition and dynamic mode decomposition." *Journal of Fluids and Structures*, 49, 53–72.

Zhao, Y., Zhao, M., Li, X., Liu, Z., and Du, J. (2019). "A modified proper orthogonal decomposition method for flow dynamic analysis." *Computers & Fluids*, 182, 28–36.